

POLITECNICO DI TORINO

Master's Degree in Biomedical Engineering



**Politecnico
di Torino**

Master's Degree Thesis

Software design and integration for a
dual-modality OC-PAM imaging device

Supervisors

Prof. Kristen Mariko MEIBURGER

M.Sc Giulia ROTUNNO

Prof. Mengyang LIU

M.Sc Adam APRO

Candidate

Giulio CARMASSI

March 2025

Summary

Today one of the main open challenges in cancer treatment is the presence and growth of drug-tolerant persister cells. Innovative studies across multiple scientific fields, such as medicine, biology and biomedical engineering, are being conducted to deepen our understanding of these cells. This thesis presents a contribution to the development of a dual-modality imaging system within the context of the REAP European project, which aims to utilize multiple contrast-enhanced optical techniques to detect and characterize rare cancer cells in therapy-resistant breast cancer models using genetically engineered organoid-based murine mammary tumors.

Specifically, this work focuses on the design and implementation of the software architecture required to acquire images using photoacoustic microscopy (PAM) and optical coherence microscopy (OCM) modalities with micrometric resolution. Achieving this result involved integrating multiple software packages and hardware components provided by project partners, ensuring precise system synchronization, and optimizing image quality. For this purpose, an innovative microring resonator (MRR) was employed as the sensor for PAM, necessitating a tunable laser and photodiode for signal readout. For OCM, which operates in the spectral domain to maximize acquisition speed, a spectrometer captures interference fringes generated by the combination of light from the sample and reference arms. A field programmable gate array (FPGA) controls the scanning pattern of the galvanometers and triggers all components. Python was chosen as the primary programming language to ensure cross-platform compatibility without specific licenses and to maintain readable, modifiable code. The software architecture

features a graphical user interface (GUI) for easy selection of acquisition parameters and a set of functions leveraging various hardware APIs to operate the system. Both modalities include preview options to verify the correct sample positioning. Moreover, custom-made scripts reconstruct and process the images, applying averaging for PAM and k-linearization for OCM as well as other de-noising techniques, using GPU for accelerated parallel processing. At last, integration with 3D Slicer allows for visualization of acquired images and volumetric data. Multiple tests were done to validate the software by performing mock acquisitions and measuring the inputs and outputs of the different components. Preliminary imaging sessions were conducted to evaluate image quality and overall system usability for its intended purpose. Software performances for scanning routines were evaluated in terms of speed, guaranteeing an acquisition rate of 30 kHz, which is the maximum possible within the limits of the hardware. The processing pipeline for OCM was also validated on data from the first system's acquisitions and external datasets, demonstrating the software capability to reconstruct, visualize and save full volumes in less than 2 minutes. In the future, this system will enable fast and advanced studies, unlocking new possibilities such as real-time visualization and analysis of persister cells during in vitro investigations.

Table of Contents

List of Figures	VI
1 Introduction	1
1.1 Optical Imaging in biomedical research	1
1.2 PAM and OCM imaging theory	1
1.2.1 PAM	1
1.2.2 OCM	4
1.3 The REAP project	5
1.4 Project's objectives and steps	6
2 Hardware components	7
2.1 Shared hardware	8
2.1.1 Galvanometric mirrors	8
2.1.2 FPGA	9
2.2 PAM system	10
2.2.1 MRR and photodiode	10
2.2.2 Lasers	11
2.2.3 DAQ	12
2.3 OCM system	13
2.3.1 Spectrometer	13
2.3.2 Laser and optics	14
3 Software development	17
3.1 Coding Language Choice	17
3.2 Interfacing with the FPGA	17
3.3 Scanning pattern	19

3.4	Laser Control	20
3.5	Previews	21
3.6	Data Acquisition	21
3.7	Data Processing	22
	3.7.1 PAM Processing	22
	3.7.2 OCM Processing	22
3.8	3D Slicer Integration	24
4	Results and Discussion	28
4.1	Hardware tests	28
4.2	Acquired volumes and images	31
	4.2.1 PAM	31
	4.2.2 OCM	34
4.3	Graphical User Interfaces (GUIs)	39
4.4	Performance evaluation	41
	4.4.1 Field of View	41
	4.4.2 Lateral resolution	42
	4.4.3 Acquisition and processing speed	43
4.5	Conclusions and Future developments	44
	Bibliography	46

List of Figures

1.1	A schematization of how the photoacoustic effect is used for imaging[4]	3
1.2	A schematization of SD-OCM	5
2.1	Schematics of the final optical design of the dual modality system including the main hardware components	7
2.2	Galvo used in our scanning system	8
2.3	The FPGA board	10
2.4	the ATS9870 DAQ board	13
2.5	Cobra-S 800 spectrometer	14
2.6	The 4 SLED laser	15
2.7	The final optical setup for the dual modality device, we can see the beam-splitter at the center with the collimators for the two laser sources and the reference arm on the right	16
2.8	Sample arm with scanning objective, we can also observe the galvos and the flip mirror on top	16
3.1	Example of a difficult to interpret acquisition routine in LabView	18
3.2	Currently implemented sawtooth scan pattern used for all acquisitions	20
3.3	Example of the application of Background subtraction to a B-scan, we can see the banding disappear	24
3.4	Flowchart of PAM acquisition software usage	26
3.5	Flowchart of OCM acquisition software usage	27

4.1	Signal from the FPGA to the galvos, we can see the fast axis in yellow and the slow one in green	29
4.2	Test of the synchronization between galvo movement and acquisition	30
4.3	Plot obtained while searching for the optimal interrogation laser wavelength	31
4.4	US wave from the gold nanofilm captured using the MRR	32
4.5	USAF 1951 target used for the first imaging sessions, the group imaged is circled	33
4.6	PAM 2x2mm image of a USAF 1951 resolution target .	34
4.7	Interference fringes recorded with the spectrometer once the system was correctly aligned and calibrated	35
4.8	B-scan preview obtained when placing a mirror in the sample arm, the line corresponds to the interference signal generated by its reflective surface	36
4.9	Maximum intensity projection of the OCM acquisition on a 2x2mm section of the resolution target	37
4.10	Maximum intensity projection of the zebra fish eye from the external dataset	38
4.11	Rendering in 3D slicer of the processed zebrafish OCM	38
4.12	User interface for OCM acquisitions	40
4.13	User interface for PAM acquisitions	40
4.14	Cross-sectional intensity profile corresponding to a FOV of 800 μm	41
4.15	6x6mm OCM maximum intensity projection of USAF 1951 target, the bright area in the middle corresponds to the FOV	42
4.16	Evaluation of the lateral resolution on the USAF 1951 target	43
4.17	Model of the 3D switch that will allow compatibility between the dual modality system and the two-photon microscopy	45

Chapter 1

Introduction

1.1 Optical Imaging in biomedical research

Optical imaging techniques are becoming prevalent in biomedical research and clinical settings thanks to their high resolution and their use of non-ionizing light radiations. These techniques are based on the interactions of photons with biological tissues. In particular, images can be reconstructed by analyzing phase shift, scattering, fluorescence or many other possible effects of incident photons that can reveal useful features. These data can be used to acquire both morphological and functional images while causing limited damage to the sample[1].

In this context, Optical coherence and photoacoustic microscopy are two emerging optical imaging technologies that can provide high-resolution (micrometer scale) three-dimensional (3D) imaging of biological tissues.

1.2 PAM and OCM imaging theory

1.2.1 PAM

The photoacoustic (PA) effect consists of a transformation from electromagnetic to mechanical energy that naturally occurs when a target hit by light releases an ultrasound (US) wave. This happens when a photo-absorbing material, after being exposed to short pulsed laser,

gets thermally excited creating internal expansion and compression waves that constitute the US wave. The intensity of these generated US waves can be calculated mathematically as (1.1).

$$p_0\vec{r} = \eta\Gamma\mu_a F(\vec{r}) \tag{1.1}$$

where η is the thermal energy conversion efficiency, Γ is the Grueneisen parameter that takes into account the local temperature of the sample, μ_a is the optical absorption coefficient, and $F(\vec{r})$ represents the light flux[2].

To obtain an image from this phenomenon we need to be able to record and quantify the resulting pressure waves. Therefore, a wide variety of detection methods are employed to convert the USs into electrical signals with the requirement of having high sensitivity over a wide bandwidth. In general, they can be divided into physical transducers that directly translate the mechanical input into current or potential differential, and optical detectors that use optical resonators to find the incident elastic waves. Physical transducers are generally made out of piezoelectric materials such as piezoceramics or crystals. Currently, this kind of sensor is the most commonly used in PA imaging applications thanks to its good performances for a relatively low price. However, the sensitivity of piezoelectric transducers is proportional to their size and this is a limitation in compact PA imaging systems developed for microscopy. In recent years, several different optical ultrasound sensors have been explored in PA imaging. Their main advantages include wide bandwidth, low electromagnetic interference, and high sensitivity per unit area[3]. This latter type is what has been used in this project and will be further explored during the analysis of the hardware components. In the end, by acquiring the signal generated by the chosen detector, every point in the image will have brightness proportional to the intensity of the US telling us where and in which quantity light absorbing particles are present in the sample(Figure 1.1).

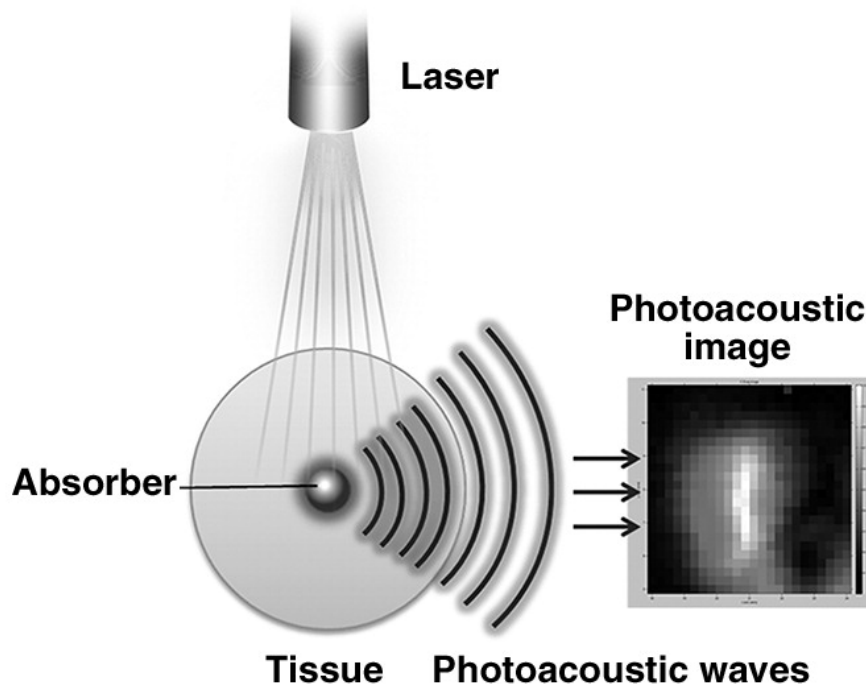


Figure 1.1: A schematization of how the photoacoustic effect is used for imaging[4]

Photoacoustic microscopy (PAM) is a particular type of PA imaging that involves exposing the sample to nanosecond long pulsed light to achieve micron-scale spatial resolution. PAM presents many advantages over other optical microscopy techniques such as confocal, two-photon microscopy, or optical coherence tomography (OCT). Mainly, PAM is not limited in penetration depth by the light diffusion limit of 1 mm in tissues since the US used to form the image suffers less attenuation by scattering than light does. Secondly, PAM can provide both structural and functional information by using for example the Doppler effect[5] or light absorbing contrast agents[6]. Lastly, PAM does not need a change in focal plane to provide a 3D image as it can operate on the same principle as a ultrasonography, hence, considering the speed of the US wave inside the medium, we can have a time-space direct correspondence. For all these reasons PAM systems can be used in many applications such as vascular biology, histology, oncology, neuroscience,

and ophthalmology[7].

1.2.2 OCM

Optical coherence microscopy (OCM) is our second optical imaging modality. OCM performs high-resolution, cross-sectional tomographic imaging of the internal microstructure in materials and biologic systems[8]. To do so a low-coherence light source is divided by a beam splitter into two separate optical paths, one that directs a portion of the laser source to the sample (sample arm) and one that sends it to a mirror (reference arm). When light is reflected back from both arms and the two beams combine once again the differences between the reflections that traveled the same path length cause an interference pattern. As a consequence, after capturing the final beam with a camera and analyzing the data obtained, we can reconstruct the presence of reflective surfaces inside our target as these will create greater interference.

There are two main types of OCM systems. The first one operates in the time domain by mechanically moving the mirror at the end of the reference arm at a constant speed. This way, the time at which we see a peak in the interference signal is proportional to the depth of the reflective surface. The second one operates in the spectral domain (SD) as it works on the frequency spectrum of the interference[9]. In SD-OCM a wide-band or swept source laser is used to provide light at multiple wavelengths, by then doing a spectral analysis of the interference beam applying the Fourier transform we can find the depth of the reflective elements in the scanned volume. The latter modality was chosen for this project as it presents the advantage that the information needed to reconstruct one A-line (one transversal line of the scanned volume) is recovered with a single camera exposure rather than over time, allowing much faster scanning (Figure 1.2). Multiple A-lines are combined to obtain one transversal section (B-scan) and all the B-scans together make our final acquired volume.

OCM is a well established technique for various ophthalmology pathologies [10] and for other fields where the low penetration depth is not a problem, such as dermatology[11].

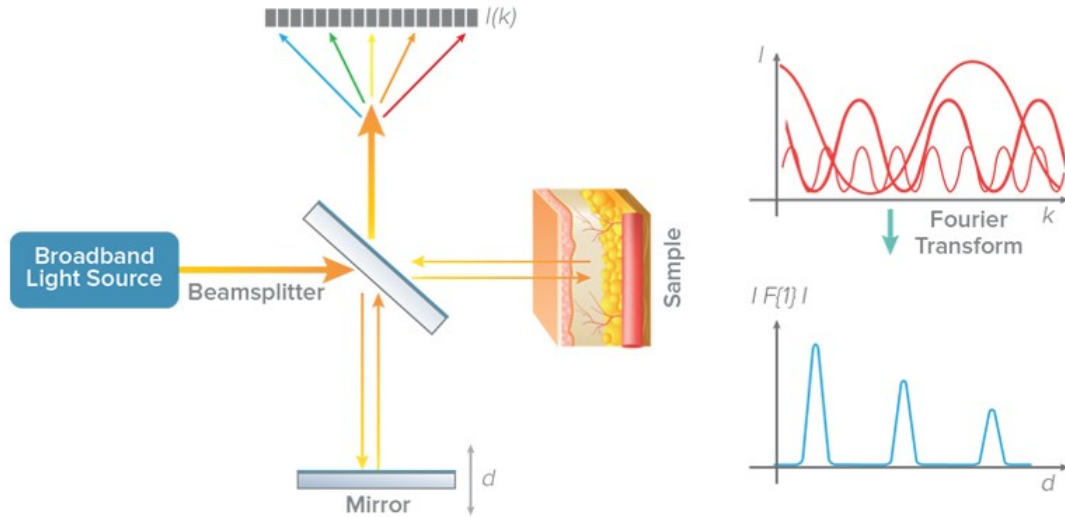


Figure 1.2: A schematization of SD-OCM

1.3 The REAP project

The REAP project is an interdisciplinary initiative aiming to detect drug-tolerant persister (DTP) cells in cancer, which contribute to therapy resistance and relapse. Funded under the H2020 program, REAP integrates expertise from multiple fields, including photonics, biology, and oncology, to develop advanced contrast-enhanced optical imaging techniques. Some of the key objectives to reach this goal include:

- Developing new contrast agents to improve imaging specificity for detecting DTP cells.
- Designing novel laser technologies for high-resolution imaging.
- Creating advanced photoacoustic sensors to enhance imaging sensitivity.

- Implementing real-time image reconstruction algorithms for efficient analysis.
- Integrating these technologies into a unified imaging system for in vitro studies.

The final imaging system will include three modalities: two-photon laser scanning , optical coherence and photoacoustic microscopy.[12]. This technology will be applied to breast cancer models to improve the understanding of DTP cell mechanisms.

1.4 Project's objectives and steps

The final device will allow for simple imaging in all three modalities by having a water filling sampling chamber to control the laser diffraction, different optical paths for the 3 lasers managed by an electronic switch-mirror and a shared scanning system. The two-photons microscopy system was completely handled independently by a partner (Milteny biotec) that also has its own software for acquisition (Inspector). For the PAM and OCM imaging the hardware and software integration were directly handled at the Medical University of Vienna in collaboration with Politecnico di Torino and will be thoroughly analyzed in the following chapters. During this project, first the necessary hardware components were gathered and analyzed. Then, Python scripts were developed to pilot the system basic functions. After validating these programs, all software functionalities were put together in user interfaces to enable easy and controllable acquisition, processing and visualization routines. In the end, it was possible to perform the first imaging session with the dual modality system and to evaluate the results.

Chapter 2

Hardware components

The following diagram (Figure 2.1) represents the complete final design of the dual modality imaging system which was based on other systems developed in the Center for Medical Physics and Biomedical Engineering of the Vienna Medical University[13].

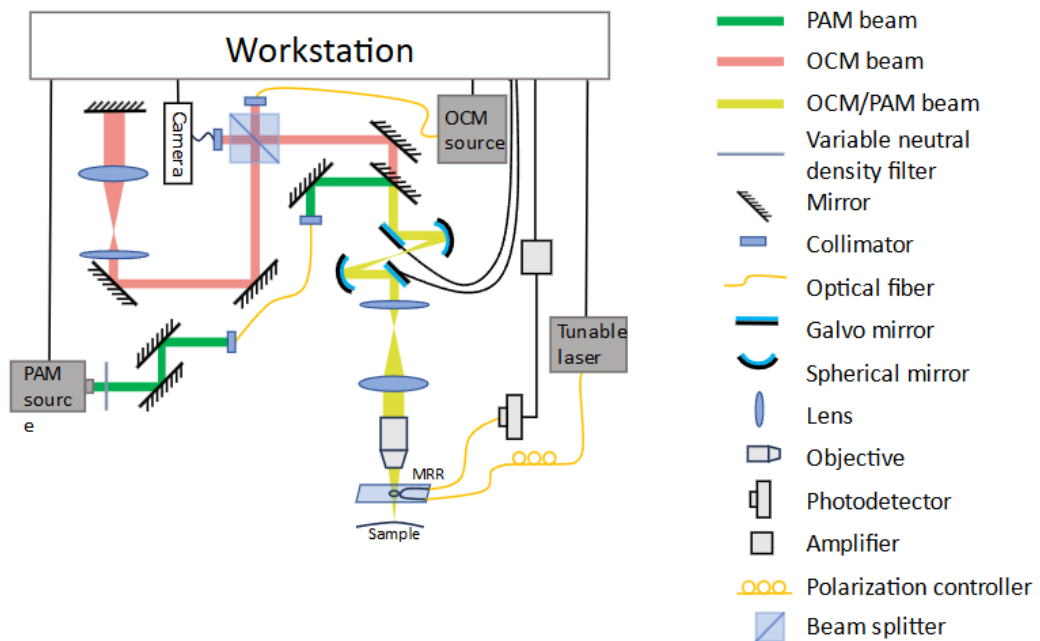


Figure 2.1: Schematics of the final optical design of the dual modality system including the main hardware components

In this chapter, all of its fundamental hardware components will be discussed with particular emphasis on the relevant specifications and their impact on the final imaging performances.

2.1 Shared hardware

2.1.1 Galvanometric mirrors

The galvanometric mirrors (galvos) consist on mirrors mounted on top of piezoelectric crystals that generate torque proportional to the voltage provided to them(Figure 2.2). The rotation of the mirrors changes the sampled position and so by varying the voltage coming into them we generate our scan pattern. The two mirrors used are referred to as the fast axis and the slow axis because the first is moved for every point, while the latter just at the end of each line to go to the next one. The galvos used in the system provide a range of motion between 27.5 and -27.5 degrees for bias levels between 10 and -10 V. This combined with the known focal length of our objective let's us calculate the position-voltage correspondence using Formula2.1:

$$\text{Voltage Output} = \frac{\text{Voltage range}}{\text{Angle range}} \times \left(\frac{180}{\pi}\right) \times \tan\left(\frac{\text{Scanning Position}}{\text{Focal Length}}\right) \quad (2.1)$$



Figure 2.2: Galvo used in our scanning system

2.1.2 FPGA

A Field programmable gate array (FPGA) is functionally the heart of the device. It consists of a hardware component with multiple input and output pins and internal processing logic optimized to run parallel loops with deterministic timings. This last characteristic in particular could not be guaranteed through programmatic commands directly from the PC and could hinder the acquisition quality massively by mismatching the acquired signals from the galvos positioning, thus creating blurred or incorrect images. This complete system synchronization is guaranteed by the FPGA by handling four main tasks:

1. Send an analog output voltage to the galvos to set the scanning position
2. Send a digital signal to trigger the acquisition of the OCM spectrometer
3. Send a digital signal to the excitation laser control box to generate a pulse
4. Send a digital signal to trigger the DAQ board for PAM acquisition

In our imaging system the PCie-7568 board from National Instruments (Figure 2.3) is used for these purposes. The only limitation encountered using this board was the maximum sampling speed of 1 MS/s for the input analog channels which does not allow to detect the photoacoustic signal since its main component frequency is around 50 MHz. Therefore, a separate dedicated acquisition board was needed for PAM imaging. The main advantage of this board is that, while most of these advanced hardware components require specific and complex programming languages to operate them, it can be entirely programmed in LabVIEW to setup input and output channels and internal logic.



Figure 2.3: The FPGA board

2.2 PAM system

2.2.1 MRR and photodiode

As previously mentioned, a PAM system needs a detector for the US waves generated by the PA effect. In particular for this system an optical-based detection method was chosen to achieve enhanced performances in terms of sensitivity and resolution. In fact, the MRR [14] is one of the most innovative components that is being developed for the REAP project. While its construction is being perfected we are using the one built by Northwestern University[15].

The MRR is made by a linear optical fiber combined with a ring shaped wave guide, the two are separated by a low-dielectric gap. The fiber serves as the input and output for the light, the light transmission to the ring waveguide is accomplished by evanescently tunneling across the low-dielectric gap. This physical phenomenon causes the beam to be coupled to the ring wave guide and bounce inside of it before going back to the fiber leading to a strong optical resonance. This resulting

optical resonance can be characterized as a huge dip in light transmission through the fiber due to destructive interference that happens inside the ring for a specific wavelength. Leveraging this strong optical resonance, the soft polymeric material of the MRR can be used as an ideal US detector as the pressure waves hitting it will cause a deformation. This change in geometry and refractive index by consequence creates a significant shift in the light wavelength corresponding to the resonance peak. Using a narrow-band laser source that will be called interrogation laser, such a shift of the resonance peak can be measured as the variation of the transmitted beam at the given wavelength. The polymeric material being transparent is also crucial for our application as the light from the PAM and OCM source will have to pass through it before hitting the sample. Therefore an opaque material could cause various kinds of shadows and artifacts in our final images. We can then use a photodiode to measure this change since it will generate an output voltage signal proportional to the intensity of the light that hits the sensor. The photodiode is DC-coupled to the output of the MRR and its output is passed through a 10 kHz to 98 MHz band-pass filter to keep only the signal relevant for the US waves and amplified.

2.2.2 Lasers

Two lasers are necessary for the PAM system. The interrogation laser mentioned before is the one that constitutes the input for the MRR fiber. The second one is called the excitation laser or PAM source and sends pulses to the sample to generate the photoacoustic signal.

The interrogation laser is motor controlled, that means that we are able to programmatically change the output wavelength in a very precise and stable manner by moving a mirror inside the laser cavity. It is fundamental to have this capability so that we can set the set on the optimal value to observe the MRR resonance shift and so obtain the maximum sensitivity. For this project, we are using the SACHER Motorized Tunable Littman/Metcalf Laser System. which provides wavelength ranges from 745 to 785 nm with fine tuning precision and high power up to 60 mW. A three-paddle polarization controller was

also added to the tunable laser output to guarantee better stability during the MRR readouts. For the final system the excitation laser will be custom made from picophotonics, from the Optoelectronics Research Center at the Tampere University, focusing on the development and manufacturing of Q-switched microchip lasers based on proprietary semiconductor saturable absorber mirror (SESAM) technology. The great contribution of this innovative technology is the nanosecond long pulses provided which allow for great resolution. Unfortunately its internal pump time that would cause very unreliable jitter, and great power output instability don't allow us to use it yet. Right now the the SOL Compact Q-switched DPSS Laser at 532 nm produced by Bright Solutions is being used. It is a green light laser that emits short, high-energy laser pulses, making it particularly suitable for applications requiring precision and power. The power and frequency of the pulses can be controlled through a dedicated digital control box which also allows external triggering. Even our substitute PAM source presents some limitations as it is not trivial to provide nanosecond long laser pulses with consistent power and timing. In fact, to obtain a stable excitation we have to maintain at maximum a 50 kHz repetition rate.

2.2.3 DAQ

The DAQ is used to acquire the data from the analog voltage signal coming from the photodiode, we need high sampling rate to correctly reconstruct the PAM image since the frequency of the ultrasounds is in the order of 50 MHz. The card presents 2 input channels, an external trigger which is very important for the system synchronization, internal memory buffers to temporarily store the acquired data. Multiple parameters can be set such as sampling rate and input resistance. We are using the AT9870 board from AlzarTech.[Figure 2.4]



Figure 2.4: the ATS9870 DAQ board

The main advantage of this kind of board is the very high sampling rate, up to 1 GS/s, as well as the high transfer rate to PC memory, up to 1.6 GB/s. Most importantly for our application, its internal memory buffer structure, of up to 4 GB allows to do real-time data acquisition as you are able to access and work on the acquired data while other samplings are in progress.

2.3 OCM system

2.3.1 Spectrometer

As we are operating in spectral domain OCM we need a spectrometer to acquire the spectral components of the light output from the interferometer. A spectrometer is a camera combined with dispersive elements that convey single wavelengths of the input light to every photosensor placed in a linear array. The Cobra-S 800 from Wasatch Photonics was the one used for this system. It has a bandwidth of 180 nm with a central wavelength of 835 nm which is optimal for our broadband laser source. Calibration was already performed on the camera by the production company which provides an equation to match each pixel to the corresponding wavelength value. This model is also very cost effective as its USB connection to the PC does not require the use of

a costly video capture card. The PC communicates directly with the camera allowing settings control, acquisition start and data transfer. Most importantly, for the system to be effective in image acquisition the spectrometer has to be set to external trigger, to guarantee synchronization, and the exposure time has to match our wanted acquisition rate. Another 6 pin IO port is present and used for the external triggering, provided as a TTL signal from the FPGA. The only limitation met using this camera is the maximum acquisition rate, because of the limits in data transfer of the USB connection the max line scan rate is 100 kHz while keeping full pixel depth of 12 bit. This value is still high enough to make scans in reasonable time also considering the speed limitations that we would have anyway for proper galvo positioning and proper functioning of the other components. Cobra spectrometers receive light input via a single-mode fiber connected with an FC/PC connector.



Figure 2.5: Cobra-S 800 spectrometer

2.3.2 Laser and optics

For the OCM the laser source used is the combination of 4 superluminescent diodes (SLEDs) from Exalos[Figure 2.6]. This generates a beam with wide light wavelength bandwidth from 760 to 880 nm. This kind of lasers is based on a p-n junction which, when biased in the forward direction, becomes optically emitting with varying powers and wavelength based on the active material composition and current level.

The light is fed into a 70:30 beam splitter and mirrors are used to form the sample and reference arm that must have a perfectly equal optical path length for the interference to occur correctly, lenses and objectives with the same optical dispersion are also placed in both arms to avoid later software compensation on the post-processing side. A variable density filter is also added to the reference arm, this circular glass piece is coated with photoabsorbant material to be able to adjust the beam power to be balanced between the two arms. Collimators with parabolic silver mirrors are used in the whole setup to get light from the fiber-coupled laser sources to free space and then couple it back into optical fiber as input for the spectrometer. These components also require the use of multiple silver-coated mirrors to direction and couple the light beams correctly.



Figure 2.6: The 4 SLED laser

To align the system a power meter is used to verify the coupling efficiency of the various collimators and the reference arm mirrors are mounted on a stage and fixed on suspended arms to easily adjust the total path length. Moreover, a low power, visible alignment laser is used to safely and easily align all the mirrors to avoid distortion of the beam shape and efficiency loss. In the final setup a flip mirror was also added to enable switching between the PAM and OCM source.(Figure2.7,2.8)

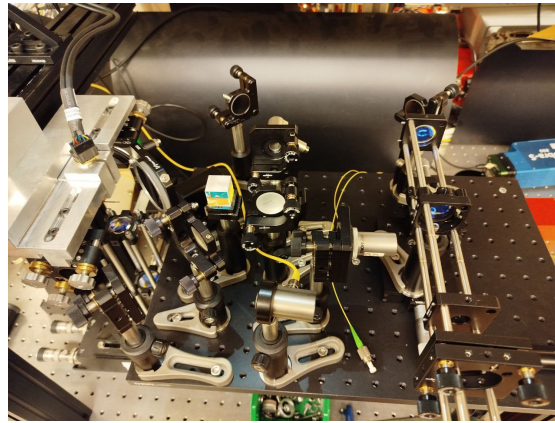


Figure 2.7: The final optical setup for the dual modality device, we can see the beam-splitter at the center with the collimators for the two laser sources and the reference arm on the right

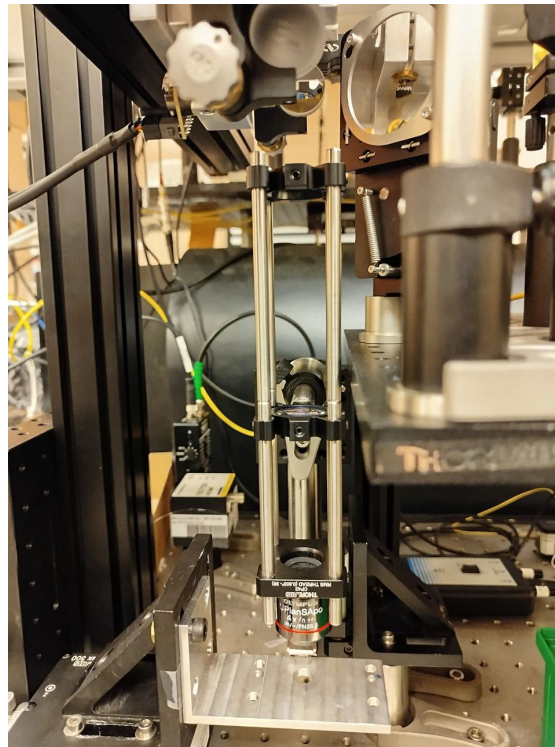


Figure 2.8: Sample arm with scanning objective, we can also observe the galvos and the flip mirror on top

Chapter 3

Software development

3.1 Coding Language Choice

The first step in designing and implementing the system was selecting an appropriate programming language. Many similar systems use LabVIEW because it offers a range of pre-built virtual instruments for interfacing with hardware components. However, since the final system must integrate with an existing machine that already utilizes a Python interface, Python was chosen as the primary language.

A common misconception is that Python scripts are too slow and inefficient to execute high-frequency synchronized acquisition routines. However, performance issues can be mitigated by utilizing C++ Directly Linked Libraries (DLLs) to communicate with hardware components and leveraging GPU parallelization for processing. This approach enables near real-time acquisition and processing. Additionally, transitioning acquisition routines from LabVIEW to Python improves code portability (Figure 3.1) and eliminates the need for an expensive LabVIEW license.

3.2 Interfacing with the FPGA

The FPGA must first be programmed using LabVIEW as previously explained in the hardware section. Once the code is compiled a bitmap

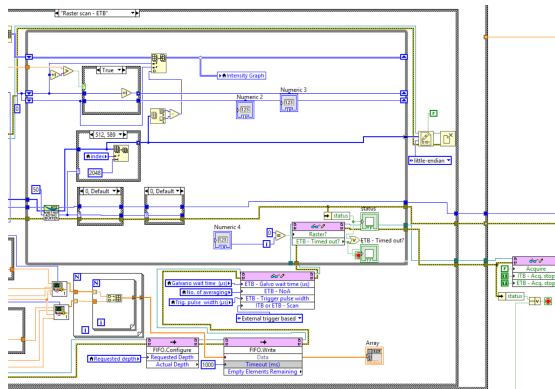


Figure 3.1: Example of a difficult to interpret acquisition routine in LabView

file is generated containing all the data concerning the set internal logic of the FPGA. This file can then be accessed by in Python through the NIFPGA API. This functionality is leveraged in our code for multiple purposes. For example, The scanning region and corresponding voltage values are calculated and loaded into the FPGA's internal memory. Similarly, parameter registers are set, and scanning routines are initiated to handle acquisition triggers.

The FPGA operates in two main states:

- Raster Mode – Controls the output voltage to the galvanometers and generates acquisition triggers for the camera or acquisition board to do a full scan.
- Acquire Mode – Generates triggers solely for the sensors to obtain previews of the signals.
- Warmup Mode - Only triggers the excitation laser to prepare for acquisition

Key parameters set on the FPGA include the number of averages for PAM, initial wait time to guarantee correct system setup, and triggering period, which directly influences acquisition speed. All the acquisition protocols that require the use of the FPGA are contained in the "FPGA v2.py" file. In general they all follow the same structure.

First, the scanning pattern is loaded into a FIFO structure. Then in loop a coordinates couple is sent to the galvos. After a set wait time triggers are sent out to the excitation laser and DAQ for PAM modality or the spectrometer when operating in OCM.

3.3 Scanning pattern

A special dedicated GALVO.py module was made to define the scanning pattern from the user given parameters: both axis starting position, ranges and focal length, according to the previously mentioned Formula 1.1. Controls were also implemented to warn the user and stop the acquisitions in case the selected positions would end up outside the range of motion of the galvos. This function currently generates a sawtooth pattern (Figure 3.2) for the scans that could be, in the future, changed if other patterns were needed.

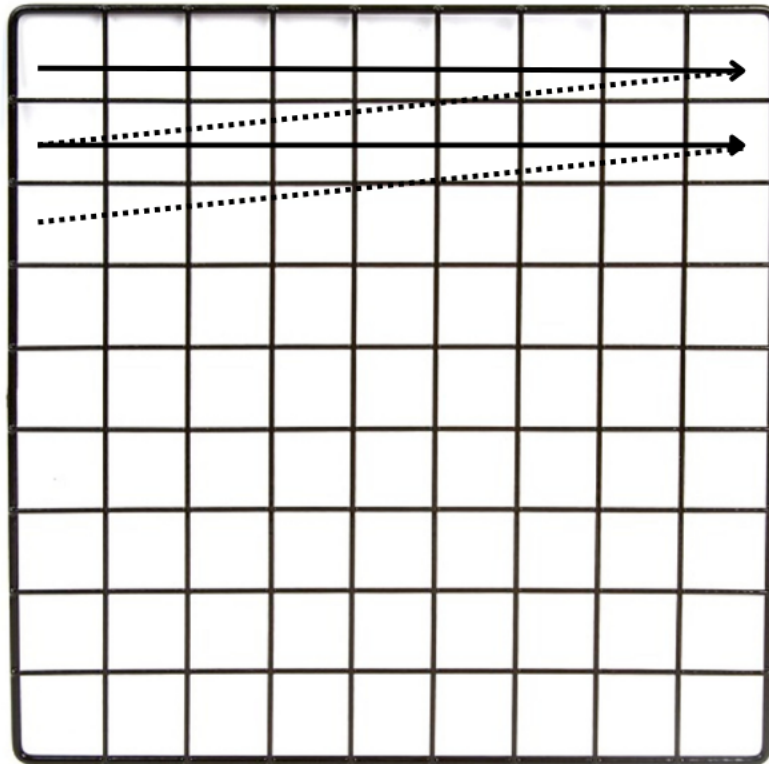


Figure 3.2: Currently implemented sawtooth scan pattern used for all acquisitions

3.4 Laser Control

The SACHER motor control API allows dynamic adjustments of the interrogation laser's wavelength directed at the micro-ring resonator (MRR) through the introduction of the MOTOR class object. A dedicated subroutine is implemented to locate the resonance peak by gradually increasing the laser wavelength while simultaneously acquiring photodiode signals via the DAQ system. The obtained curve is then numerically differentiated to identify the maximum slope, ensuring optimal placement of the interrogation laser. This guarantees maximum sensitivity to photoacoustic ultrasound waves, as peak shifts result in

significant changes in transmitted light.

3.5 Previews

Before initiating long acquisitions, it is crucial to verify signal acquisition and sample positioning. Therefore, preview functions were developed:

- For PAM, the signal from a single point at the galvos' zero position is visualized to confirm the presence of an ultrasound wave. This feature also allows users to define the starting sample of the recording, optimizing memory usage and filtering out unwanted noise occurring immediately after excitation.
- For OCM, a similar preview function ensures correct sample positioning and acquisition settings before the full scan by plotting on screen a B-scan positioned according to the user's set starting position of the scan.

3.6 Data Acquisition

The DAQ system is central to both PAM imaging and resonance peak detection (as seen in Figure 4.3) of the MRR. The ATSAPI is used to configure board parameters, including input impedance, acquisition channels, external triggering, and buffer sizes. These functionalities are all included in the board object introduced by the API and leveraged in the various PAM subroutines of the code.

Buffers are pre-allocated memory spaces on the board, progressively filled during acquisition. This setup allows the script to access and process acquired data asynchronously while new samples continue to be collected, significantly enhancing acquisition speed. The board is configured to acquire 2048-sample buffers at a 500 Ms/s sampling rate upon receiving a trigger from the FPGA. After acquisition, scan methods automatically generate text files containing the scanning parameters used, aiding reconstruction and interpretation of results. The final

image is then directly visualized and the user is able to save it as a PNG file.

3.7 Data Processing

3.7.1 PAM Processing

For PAM data, signal amplitudes are calculated after averaging multiple acquisitions at the same position to reduce noise. This works since the signal noise acquired by the DAQ from the photodiode can be considered as statistical white noise. So since the US signal amplitude should be stable over time, since the sample is fixed and the acquisition trigger is synced with the excitation laser (no jitter) the signal should not be altered by the averaging while the noise with a mean value of 0 will tend to 0 while increasing the number of averages. In theory, the signal-to-noise ratio (SNR) improvement is proportional to the square root of the number of averages selected before acquisition begins. This can be easily achieved by sending the same coordinates to the galvos N number of times and saving N acquisitions on the same data buffer, once the buffer is filled it can be split into the different epochs and averaged to then calculate the signal amplitude as the difference between the maximum and minimum of the signal, this will be the final value saved for each position.

3.7.2 OCM Processing

Each scanning position in OCM produces a spectrum (A-line). Once a line scan is finished we have a complete B-scan that is saved in a individual binary file that still needs to be processed to obtain our final transverse cross-section image. Processing steps include:

1. Background Removal – Imperfections in the spectrometer detectors commonly cause some of the values on the A-line to be different from zero even when no light is entering the camera. This can be easily shown by acquiring a spectrum while the OCM source

is turned off as in the B-scan we will see some horizontal gray bands. To correct this phenomenon that would generate noise in our final image, an average background signal is calculated line by line horizontally and subtracted from the spectrum(Figure 3.3).

2. K-Linearization – The inverse Fourier transform is used to convert spectral data into depth profiles. However, raw data from the spectrometer are not linear in wavelength space (k-space). This would cause in the signal a broadening of the point spread especially when examining higher depths that would negatively impact the axial resolution of the system. In literature multiple studies can be found on k-linearization methods based on calibration or automatic procedures[16]. As a first approach a simple resampling of the spectrum using the predefined calibration curve provided by the manufacturer was implemented. Linear interpolation ensures that data points are evenly spaced in k-space, improving axial resolution especially at higher imaging depths.
3. Windowing – A window function is applied to the raw data, reducing the signal value outside a predefined range. This reduces side lobes in the resulting signal after the inverse fast Fourier transform (IFFT). A Gaussian window is implemented in our processing pipeline.
4. Inverse Fast Fourier Transform (IFFT) – The IFFT is used to compute the depth profile from the pre-processed spectral data. In fact, by applying the Fourier Transform to a signal in frequency we will get back a signal in the domain of time, by then knowing the speed of light each point in time can be translated to a position in space, obtaining thus finally our depth profile. To optimize performance, the NVIDIA CUDA Fast Fourier Transform library (Cupy) is utilized, enabling parallel processing of multiple B-scans. This package allows to pass the array containing each B-scan from the CPU RAM to the GPU and process it all at once in parallel loops instead of elaborating every A-line spectrum singularly.
5. Maximum intensity projection - At the end of the processing

pipeline a maximum intensity projection image is reconstructed and visualized. This kind of image is made by taking the maximum intensity value for each point in the x-y (en face) plane in the range of depth of interest. It is generally an efficient way of evaluating the success and quality of the scan without the need of a complete 3D rendering of the acquired volume.

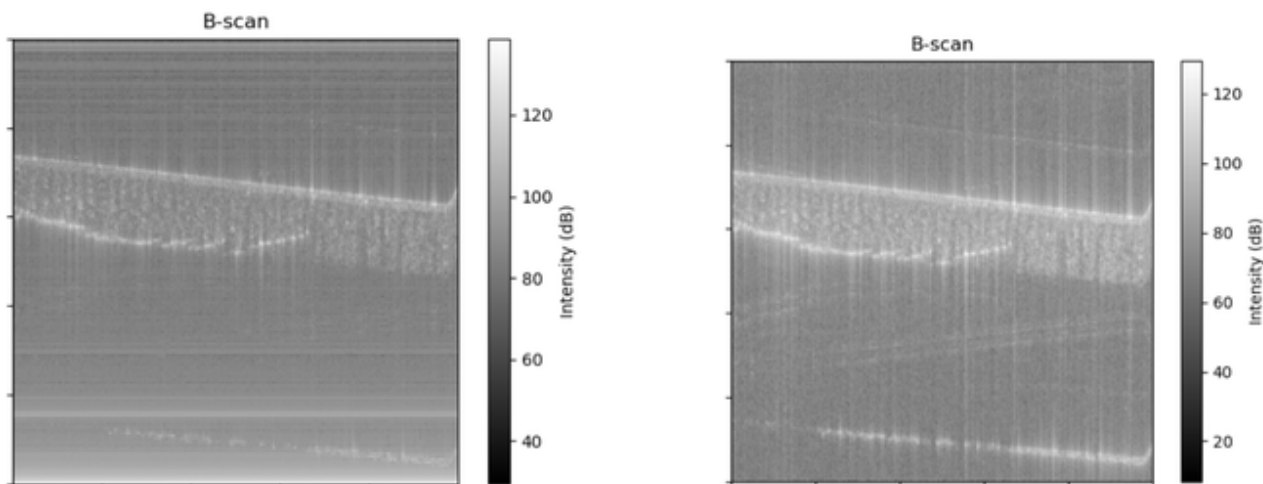


Figure 3.3: Example of the application of Background subtraction to a B-scan, we can see the banding disappear

3.8 3D Slicer Integration

Finally, an integration with 3D Slicer was introduced to provide real-time visualization of processed B-scans and reconstructed volumes. 3D Slicer is a free open-source software mainly developed to easily work on all kinds of medical tomographies. It offers many custom modules from its community as well as a Python code interface, allowing many opportunities for the creation of custom functions. This feature in particular is based on the IGT module, which facilitates seamless data transfer from the Python script to 3D Slicer by creating a server client connection between the two softwares. As soon as a B-scan is processed in Python it is sent and displayed in a 3D slicer view, once they are all

completed they get stacked together and sent as a full volume. 3D slicer then provides a wide range of functionalities to render and segment the acquisition making our sample data ready to be analyzed.

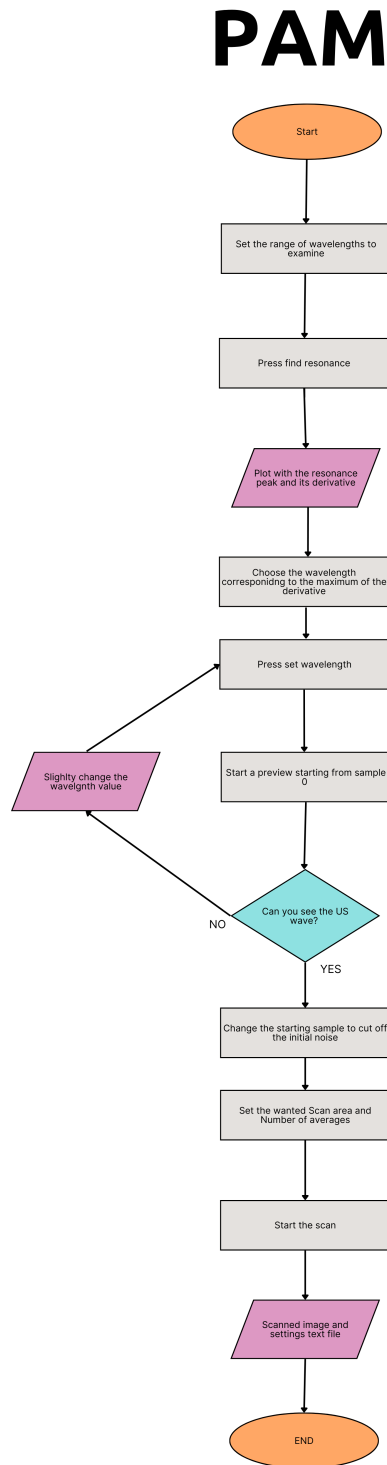


Figure 3.4: Flowchart of PAM acquisition software usage

OCM

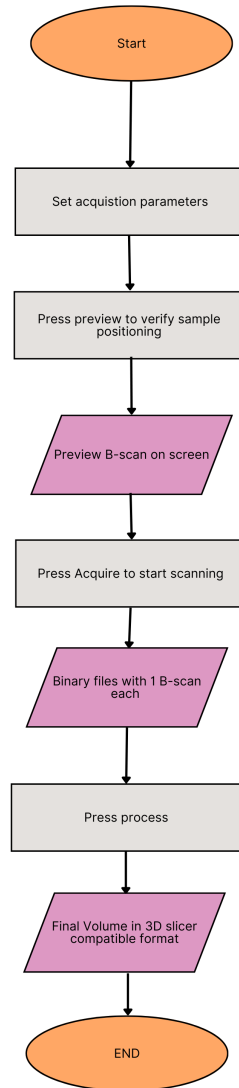


Figure 3.5: Flowchart of OCM acquisition software usage

Chapter 4

Results and Discussion

4.1 Hardware tests

As a starting point, tests were conducted on the functional core of the device: the FPGA. In particular, using an oscilloscope the output channels for the galvos and the triggers were measured to check if the correct positions were set in a synchronized manner. As Figure 4.1 shows, we can clearly see the difference between the slow and fast axis, also by reversing Formula 2.1 we can verify that the voltages correspond to our desired scan pattern. Moreover, the signal sent to the galvos was also acquired by the DAQ board to test if the acquisition will get triggered correctly for every position change as we want during the acquisition routines(Figure 4.2). As we can see, for every position acquired on the same line the fast axis galvo is at a different level, once the scan goes to the next line, after 10 positions in the figure case, it starts back from the same value. When averaging is applied for PAM the same voltage value is sent to the galvos as many times as the number of averages, also the same number of triggers is sent to the DAQ. These acquisitions are then averaged and the final value will correspond to the intensity of the image in this point. This procedure was also applied in figure and as we can see the resulting voltage readouts are very smooth. Once the FPGA was connected to the Galvos and the laser source was turned it was also possible to see visually that the correct scan patten was being generated. After successfully proving this, the



Figure 4.1: Signal from the FPGA to the galvos, we can see the fast axis in yellow and the slow one in green

external triggering of the spectrometer was validated using the company software and checking if the frames per second acquired corresponded to the wanted acquisition frequency set on the FPGA. This test was successful as well trying different speeds up to the maximum allowed by the camera specifications (100 kHz). Calibration tests were also run for the interrogation laser, using the laser control code to shift its wavelength while observing the output of the MRR, the resulting data points were fitted in a lorentzian fit and derived to find the optimal value for US detection. The optimal value, which as previously mentioned is the maximum of the derivative, in this case (Figure 4.3) is 781.12 nm, which is compatible with the range indicated by the MRR designers. We can also observe in the acquired data a very sharp peak that goes almost perfectly to 0 V, this is an indicator of good quality of the MRR as it will correspond to an high sensitivity when used as our

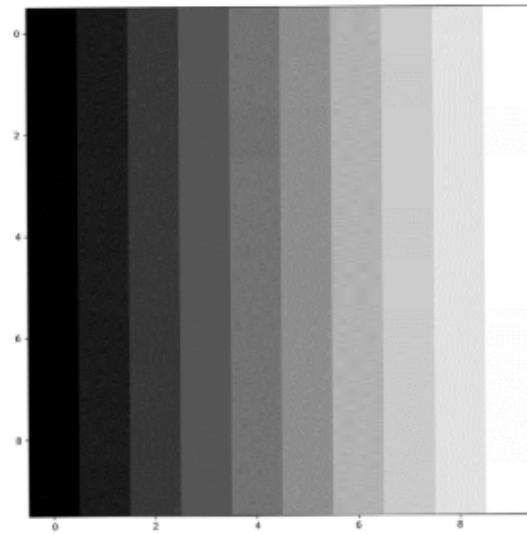


Figure 4.2: Test of the synchronization between galvo movement and acquisition

US detector. This kind of calibration needs to be performed every time before an imaging session since the changing external temperature conditions greatly influence the MRR resonance peak. Therefore, the excitation laser should also be turned on when starting an imaging session as to allow for a warm-up period and allow to calibrate in our real use conditions.

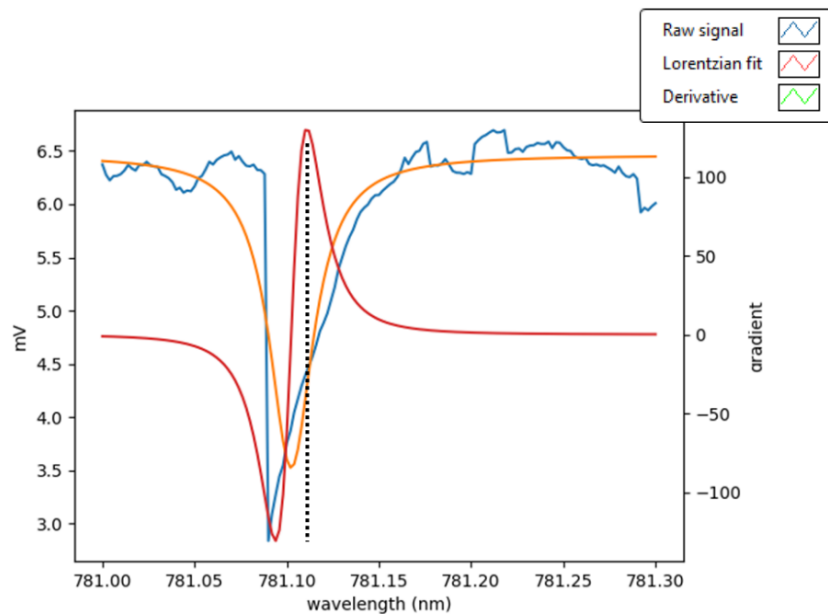


Figure 4.3: Plot obtained while searching for the optimal interrogation laser wavelength

4.2 Acquired volumes and images

4.2.1 PAM

For PAM the first tests consisted in acquiring single point signals from a homogeneous photoabsorbing material making sure the 50 kHz working repetition rate was respected. This allowed to check if the US signal could be correctly captured and to fine-tune the parameters (initial samples to discard, laser power) and optical alignment, while also doing MRR characterization and first evaluations of the image quality (Figure 4.4). The time at which the peak appears is also significant as, knowing the speed of the US wave, we can determine the depth of the photoabsorbing layer. After correctly finding this signal, first scans were acquired with success on USAF 19851 resolution targets (Figure 4.5, 4.6), this image shows a 2x2mm portion of the target where the bars width are in the range of 100 μm .

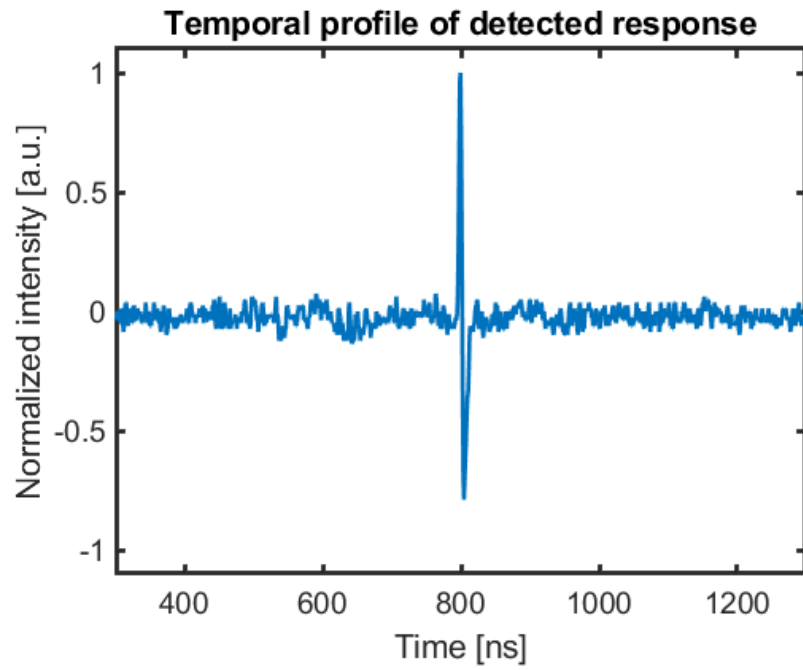


Figure 4.4: US wave from the gold nanofilm captured using the MRR

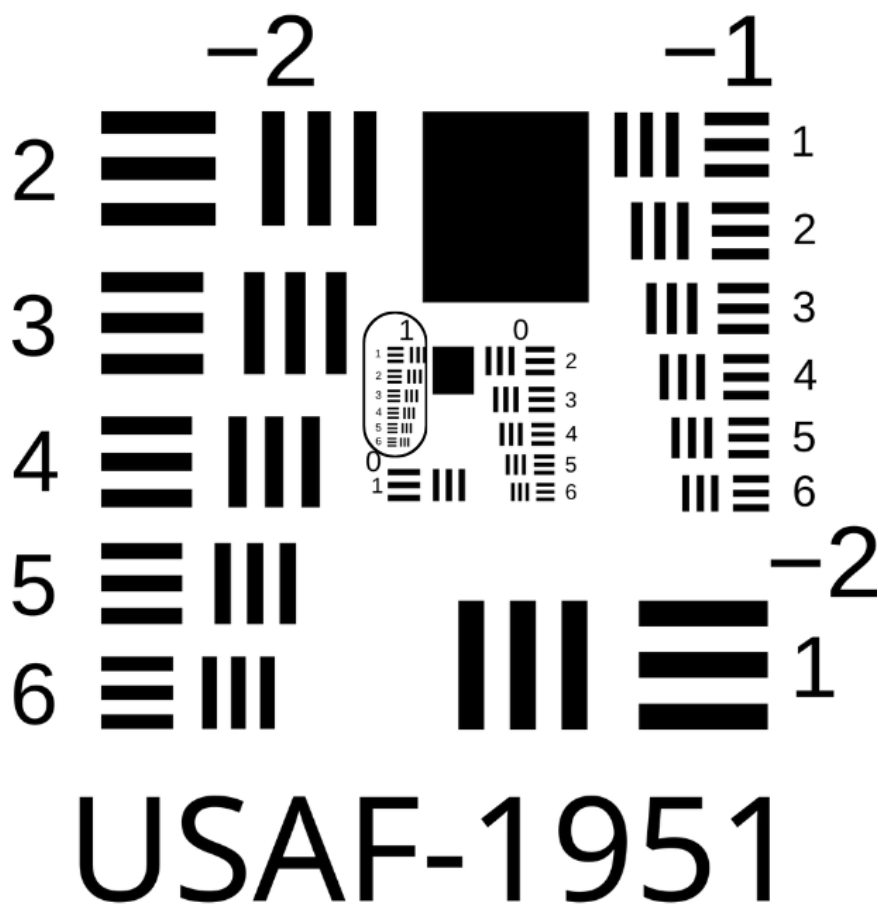


Figure 4.5: USAF 1951 target used for the first imaging sessions, the group imaged is circled

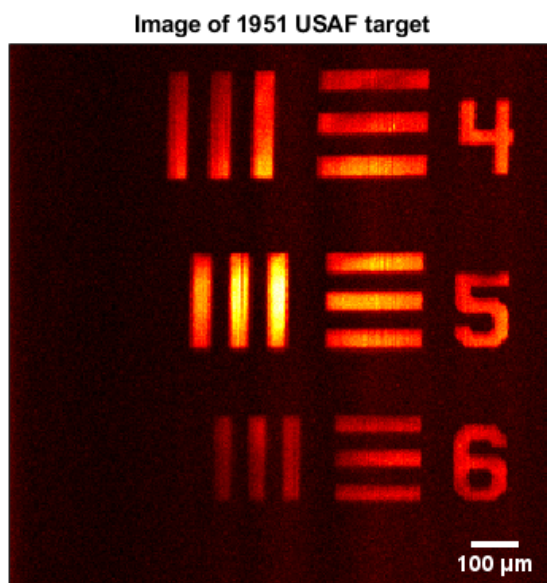


Figure 4.6: PAM 2x2mm image of a USAF 1951 resolution target

4.2.2 OCM

To get our first OCM images, first a mirror was placed at the end of the reference arm to fine tune the reference arm length and see a very clear reflection signal on the spectrometer. When this process was completed we were able to see the interference fringes recorded by the spectrometer (Figure 4.7) and the preview of a processed B-scan containing the signal from the mirror reflection (Figure 4.8). During the tuning process it was possible to observe how the mirror surface would become more blurred and undefined if the optical path lengths between the two arms did not match.

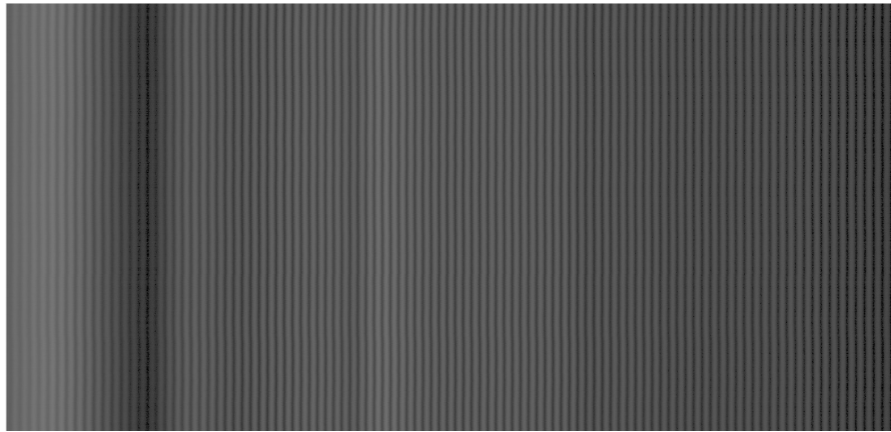


Figure 4.7: Interference fringes recorded with the spectrometer once the system was correctly aligned and calibrated

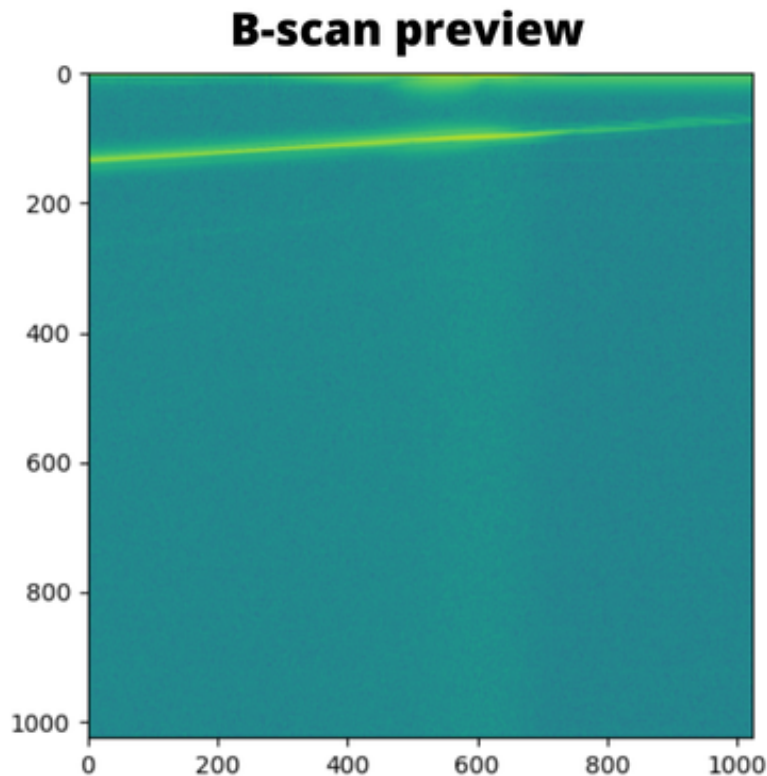


Figure 4.8: B-scan preview obtained when placing a mirror in the sample arm, the line corresponds to the interference signal generated by its reflective surface

Afterwards we proceeded to successfully image resolution targets (Figure 4.9) with scan parameters of 400 B-scans of 400 A-scans at a 100 kHz A-scan rate. The bars that we could see were around $150\ \mu\text{m}$ wide but with further imaging session it is plausible that even smaller ones will be able to be imaged. This was still a promising result for the overall project as for the first it was possible to obtain OCM images using our particular spectrometer and galvo scanner setup. The processing pipeline was also validated on a more complex external zebrafish dataset proving its correct functioning (Figure 4.10). The final tomograms obtained from these data were also used to test the functionality of the 3D slicer integration obtaining some rough

renderings (Figure 4.11).

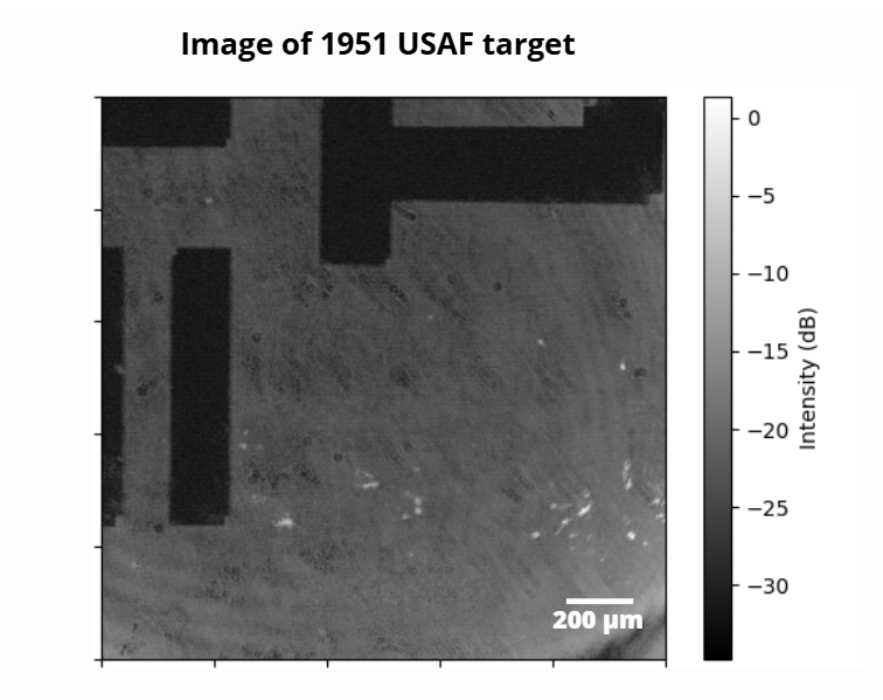


Figure 4.9: Maximum intensity projection of the OCM acquisition on a 2x2mm section of the resolution target

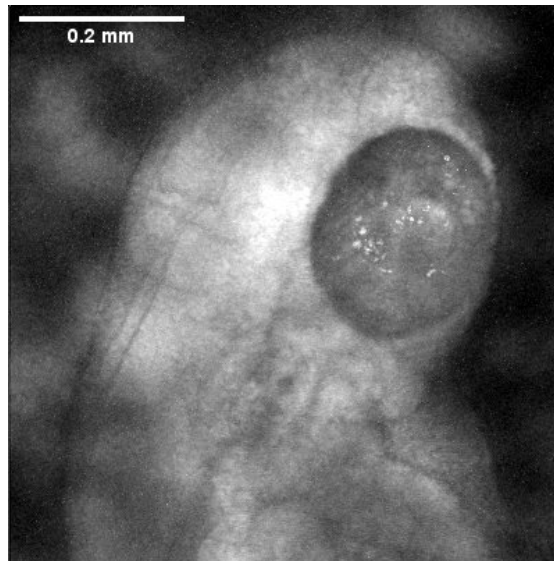


Figure 4.10: Maximum intensity projection of the zebra fish eye from the external dataset

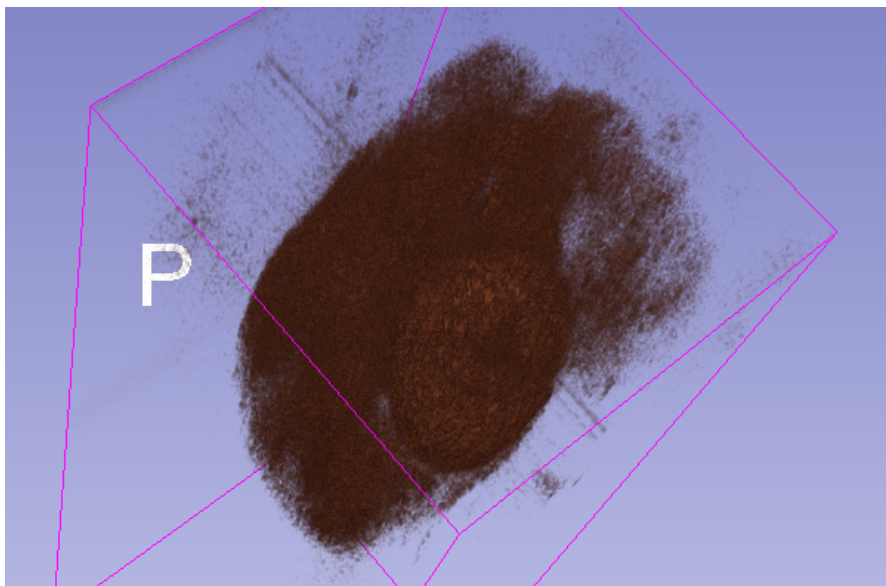


Figure 4.11: Rendering in 3D slicer of the processed zebrafish OCM

4.3 Graphical User Interfaces (GUIs)

The final result of the software integration were two basic graphical user interfaces (GUIs) developed to simplify parameter configuration and image acquisition for both modalities. Users using these programs can:

- Select the scanning region by setting the starting positions and scanning ranges.
- Define the number of A-scans and B-scans (for OCM).
- Set interrogation laser parameters (for PAM).
- Get preview signals.
- Set the initial signal portion to discard (for PAM).
- Choose a destination folder and acquisition series code.
- Start acquisitions.
- Start the processing routine (for OCM).

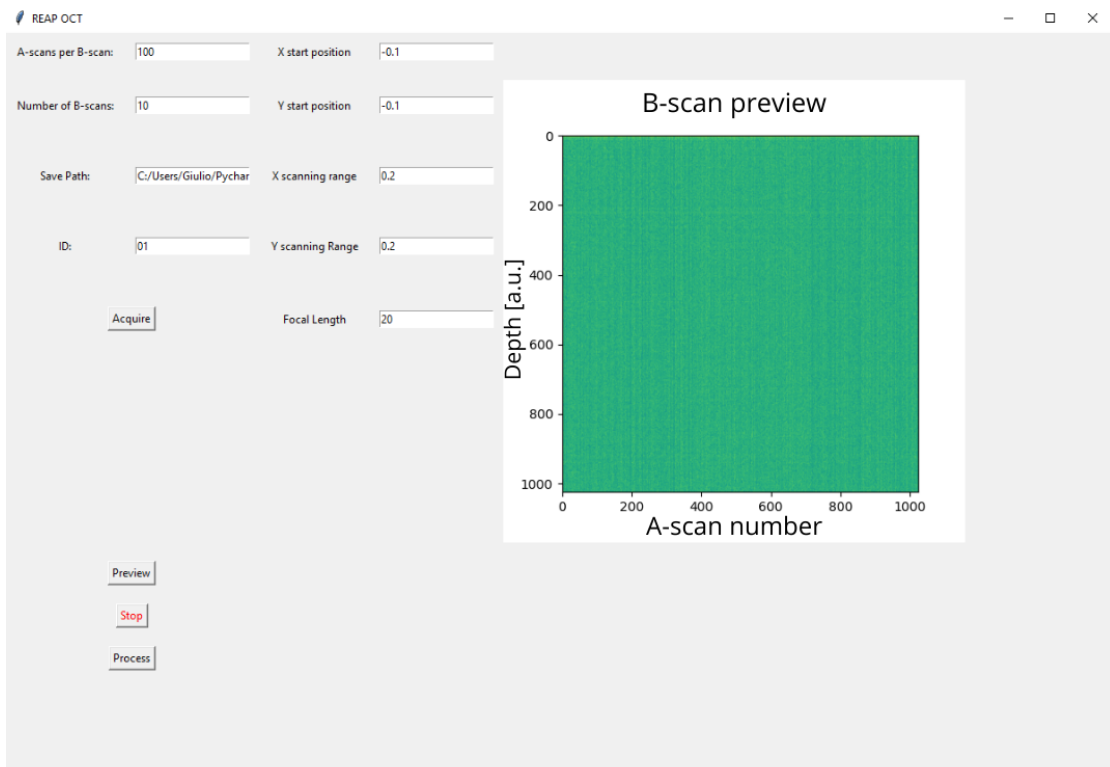


Figure 4.12: User interface for OCM acquisitions

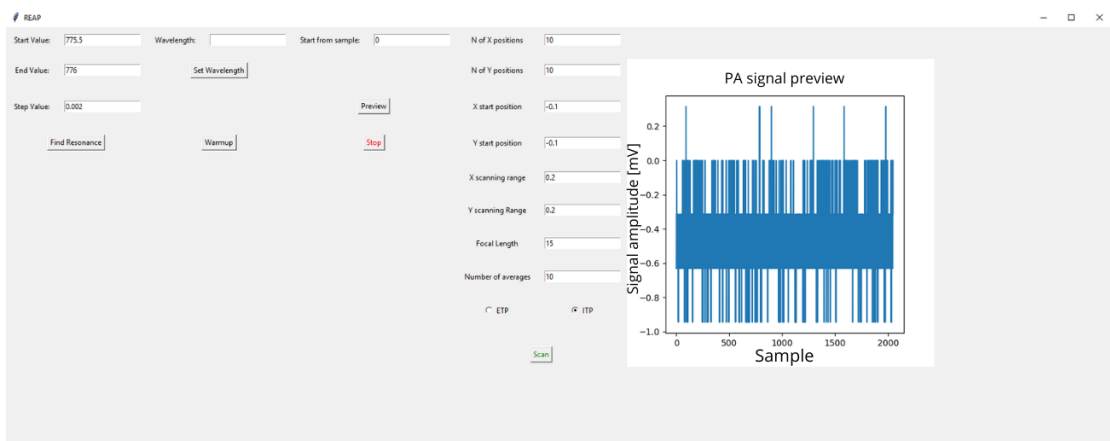


Figure 4.13: User interface for PAM acquisitions

4.4 Performance evaluation

4.4.1 Field of View

The field of view (FOV), which is the maximum area we can image, was experimentally evaluated for both modalities. For PAM, this was done by imaging a uniformly absorbing USAF target and evaluating the cross-sectional intensity profile (Figure 4.14). This highlighted how the limiting factor for this modality is the MRR, which can correctly record the PA induced US waves only in a section of $800 \mu\text{m}$ around its center. This value is still compatible with the final project objective of cellular imaging. For OCM, the evaluation of the OCM was done by

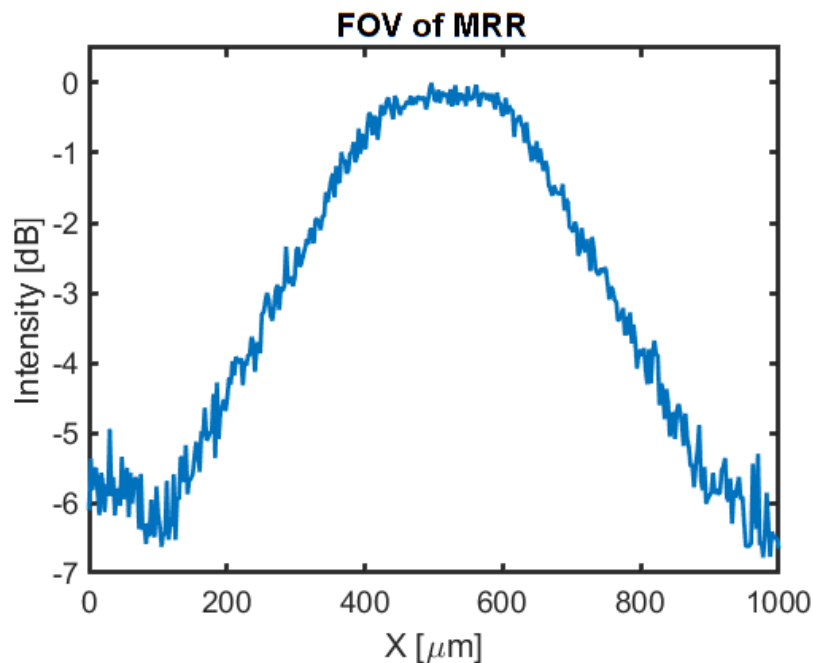


Figure 4.14: Cross-sectional intensity profile corresponding to a FOV of $800 \mu\text{m}$

imaging a larger area of the resolution target of $6\text{mm} \times 6\text{mm}$. Since in this case we are only limited by the objective it was easy to observe that we could get the reflection signal in a section 3 mm wide without encountering distortions (Figure 4.15).

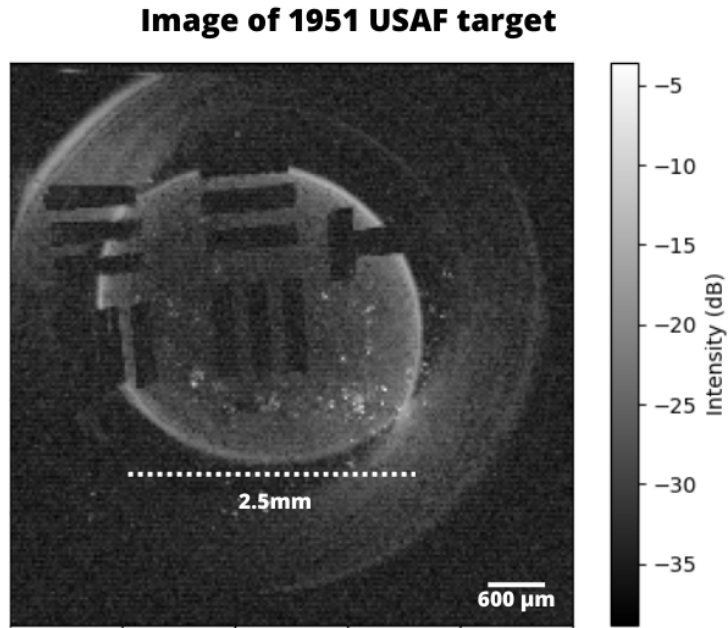


Figure 4.15: 6x6mm OCM maximum intensity projection of USAF 1951 target, the bright area in the middle corresponds to the FOV

4.4.2 Lateral resolution

Lateral resolution represents the system capability of distinguishing different elements placed side by side in the image. This was the main parameter evaluated while considering image quality because it determines the scale of cell features we will be able to see in our final application. For PAM, it was measured by imaging a sharp edge of a 1951 USAF target with the excitation source operating at 40 kHz repetition rate and using 25 nJ pulse energy on the sample. In Figure (4.16), the full width at half maximum (FWHM) of the line spread function (LSF) shows a measured lateral resolution of 3 μm .

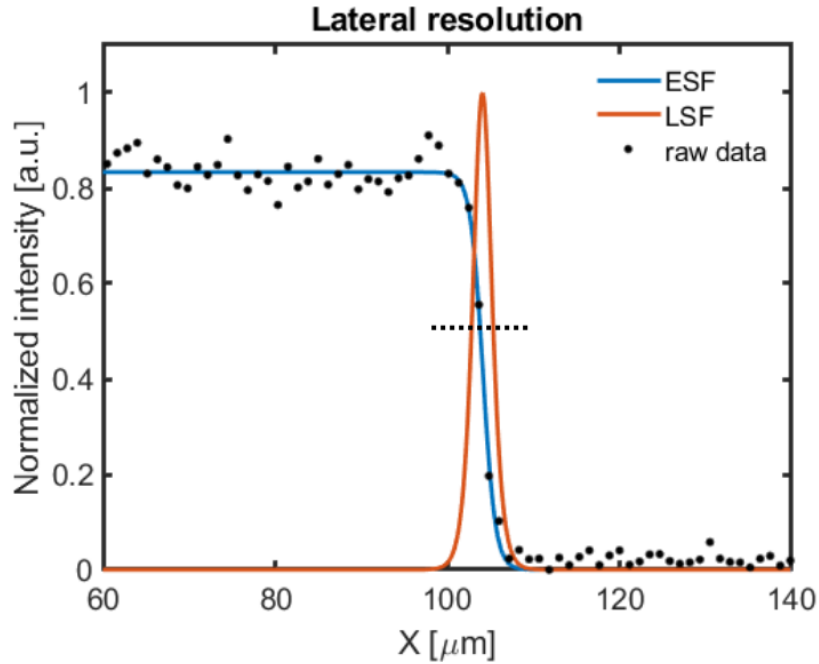


Figure 4.16: Evaluation of the lateral resolution on the USAF 1951 target

The same procedure was also applied to the OCM on a 1x1mm image of the same target obtaining a lateral resolution of 5 μm .

4.4.3 Acquisition and processing speed

For PAM the acquisition rate is fixed by the hardware more than the software as the need for averaging and the fixed rate of 50 kHz determine a relatively slow data flow, allowing the software processing of the image to be completed at the same rate as the scanning progression. For OCM the extended need for post-processing application requires to be more careful about the computational speed. Fortunately, the GPU integration showed great performances being able to process volumes composed of up to 400 B-scans in 140 seconds on average. In reality, the most time consuming part of the pipeline while using the GPU becomes passing back the completely processed volume, save it to hard-drive and visualize it. Without this final step the time spent just for the processing drops down to an average of 40 seconds. For comparison

applying the same processing pipeline using CPU only can take up to 5 minutes for a single volume.

4.5 Conclusions and Future developments

In the end, this project was successful in developing high-speed synchronized imaging routines in both PAM and OCM modalities. Moreover, the user interfaces allow anyone to easily set up acquisitions with custom parameters for future experiments. All the optimizations of the different pipelines also allow the data that will be obtained using the system to be rapidly visualized and processed for further analysis.

In the future, the PAM modality could be enriched by adding more sophisticated processing techniques to correct, for example, the angular dependency on the signal. It is in fact notable that the farther away we go from the central point of the MRR the weaker the signal gets as this effect is further worsened by the laser focus of the objective lens which is stronger in the middle. This could be compensated digitally by adding a position-based gain factor similar to what is done in echographies with time gain compensation but using more refined methods based on models of the particular laser and ultrasound absorption by the scanned medium.

For OCM instead of using the linearization based on the company calibration, as some grating and camera parameters may change over time and with use, more advanced automatic pipelines could be applied based on the signal phase. Also, on the optical side, better collimation alignment could be tried to improve coupling efficiency, as of right now only around 3% of the light from the OCM source gets coupled back to the spectrometer limiting the performances. Moreover, more processing options could be added to the pipeline and made selectable from the user interface, such as the possibility of choosing other windowing options. In general, more acquisitions still need to be done to properly determine the imaging quality before proceeding to use the system for the intended biological experiments of the project.

Lastly, in the larger scope of the REAP project, the next step will be to integrate this dual modality system with the Milteny two-photon

microscopy device to obtain the final triple modality goal. For this purpose, a switch (Figure 4.17) has already been designed to enable scan control through the FPGA like in our current system. Here our choice of developing in Python will also have a big impact as once all the components will be put together, the software will just need to be copied with minor packages installation to guarantee all the same functionalities.

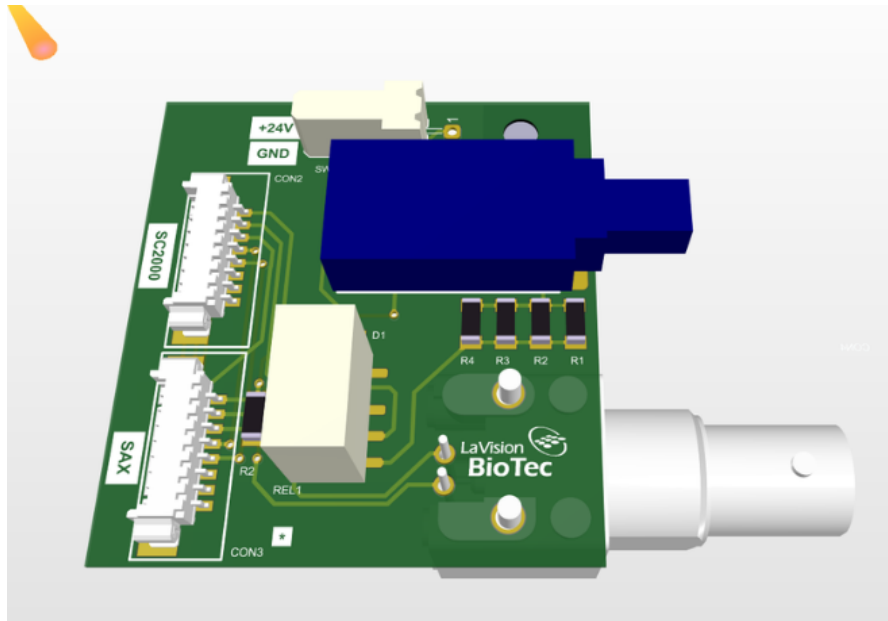


Figure 4.17: Model of the 3D switch that will allow compatibility between the dual modality system and the two-photon microscopy

Bibliography

- [1] Shuliang Jiao. *Biomedical optical imaging technology and applications: From basic research toward clinical diagnosis*. 2020 (cit. on p. 1).
- [2] Zohreh Hosseinaee, Martin Le, Kevan Bell, and Parsin Haji Reza. «Towards non-contact photoacoustic imaging [review]». In: *Photoacoustics* 20 (2020), p. 100207. ISSN: 2213-5979 (cit. on p. 2).
- [3] Liying Zhu, Hongming Cao, Jun Ma, and Lidai Wang. «Optical ultrasound sensors for photoacoustic imaging: a review». In: *Journal of Biomedical Optics* 29.S1 (2024), S11523–S11523 (cit. on p. 2).
- [4] Mohamed BenSalah. «Shape and location recovery of laser excitation sources in photoacoustic imaging using topological gradient optimization». In: *Journal of Computational and Applied Mathematics* 451 (2024), p. 116047. ISSN: 0377-0427 (cit. on p. 3).
- [5] Hui Fang, Konstantin Maslov, and Lihong V. Wang. «Photoacoustic Doppler Effect from Flowing Small Light-Absorbing Particles». In: *Phys. Rev. Lett.* 99 (18 Oct. 2007), p. 184501. DOI: 10.1103/PhysRevLett.99.184501. URL: <https://link.aps.org/doi/10.1103/PhysRevLett.99.184501> (cit. on p. 3).
- [6] Judith Weber, Paul C Beard, and Sarah E Bohndiek. «Contrast agents for molecular photoacoustic imaging». In: *Nature methods* 13.8 (2016), pp. 639–650 (cit. on p. 3).
- [7] Seungwan Jeon, Jongbeom Kim, Donghyun Lee, Jin Woo Baik, and Chulhong Kim. «Review on practical photoacoustic microscopy». In: *Photoacoustics* 15 (2019), p. 100141 (cit. on p. 4).

- [8] Aaron D Aguirre and James G Fujimoto. «Optical coherence microscopy». In: *Optical Coherence Tomography: Technology and Applications*. Springer, 2008, pp. 505–542 (cit. on p. 4).
- [9] Chengyang Xu, Claudio Vinegoni, Tyler S Ralston, Wei Luo, Wei Tan, and Stephen A Boppart. «Spectroscopic spectral-domain optical coherence microscopy». In: *Optics letters* 31.8 (2006), pp. 1079–1081 (cit. on p. 4).
- [10] Vahid Mohammadzadeh, Nima Fatehi, Adeleh Yarmohammadi, Ji Woong Lee, Farideh Sharifipour, Ramin Daneshvar, Joseph Caprioli, and Kouros Nouri-Mahdavi. «Macular imaging with optical coherence tomography in glaucoma». In: *Survey of Ophthalmology* 65.6 (2020), pp. 597–638 (cit. on p. 5).
- [11] Sattler E., Käßtle R., and Welzel J. «Optical coherence tomography in dermatology.» In: *J Biomed Opt.* (2013) (cit. on p. 5).
- [12] Mengyang Liu et al. «REAP: revealing drug tolerant persister cells in cancer using contrast enhanced optical coherence and photoacoustic tomography». In: *Journal of Physics: Photonics* (2021) (cit. on p. 6).
- [13] Mia Kvåle Løvmo, Shiyu Deng, Simon Moser, Rainer Leitgeb, Wolfgang Drexler, and Monika Ritsch-Martel. «Ultrasound-induced reorientation for multi-angle optical coherence tomography». In: *Nature Communications* (2024) (cit. on p. 7).
- [14] Li H., Dong B., and Zhang Z. et al. «A transparent broadband ultrasonic detector based on an optical micro-ring resonator for photoacoustic microscopy.» In: *Sci Rep* (2014) (cit. on p. 10).
- [15] Youngseop Lee, Hao F Zhang, and Cheng Sun. «Microring Resonator Based Disposable Ultrasound-sensing Chronic Cranial Window». In: *Biophotonics Congress: Biomedical Optics 2022 (Translational, Microscopy, OCT, OTS, BRAIN)*. Optica Publishing Group, 2022, OM2D.7 (cit. on p. 10).

- [16] Mansik Jeon, Jeehyun Kim, Unsang Jung, Changho Lee, Woonggyu Jung, and Stephen A Boppart. «Full-range k-domain linearization in spectral-domain optical coherence tomography». In: *Applied optics* 50.8 (2011), pp. 1158–1163 (cit. on p. 23).

Acknowledgements

I would like to thank everyone who supported me during this thesis's project as well as during my 5 years of University.

To Giulia and Adam and everyone who I shared my 6 months in Vienna with. You were all very kind to me and made my experience abroad great.

To my parents Dario and Antonella who always supported me in my choices. I know I can always rely on you and this certainty is what helps me reach my goals with tranquility.

To my girlfriend Anna. Your love makes me feel like I always have someone by my side even when I was away. I hope to be able to do the same for you now that you will start a new chapter of your life.

To Francesca and Federico who had the patience of living with me in Turin. We have known each other for our whole life and it is great to see that we all are moving forward in our achievements.

To all my friends. Even if I am awful at keeping in touch, I always cherish the moments we spend together and I am glad to share with you the end of this journey.